Available online at www.sciencedirect.com
ScienceDirect
Trans. Nonferrous Met. Soc. China 31(2021) 1113−1126
Transactions of Nonferrous Metals Society of China
www.tnmsc.cn

Efficient destruction of sodium cyanide by thermal decomposition with addition of ferric oxide

Kai-wei DONG[1], Feng XIE[1], Wei WANG[1], Yong-feng CHANG[1], Chun-lin CHEN[2], Xiao-wei GU[3,4]

1. School of Metallurgy, Northeastern University, Shenyang 110819, China;
2. CSIRO Minerals Resources, Clayton, Victoria 3168, Australia;
3. School of Resources and Civil Engineering, Northeastern University, Shenyang 110819, China;
4. Science and Technology Innovation Center of Smart Water and Resource Environment, Northeastern University, Shenyang 110819, China

Received 30 April 2020; accepted 22 November 2020

Abstract: Efficient destruction of cyanide by thermal decomposition with ferric oxide addition was proposed. The mechanism of destruction of sodium cyanide with or without ferric oxide addition under various conditions was examined by XRD, DSC−TG, and chemical analysis technologies. In the absence of ferric oxide, sodium cyanide decomposes at 587.4 °C in air and 879.2 °C in argon atmosphere. In the presence of ferric oxide, about 60% of sodium cyanide decomposes at 350 °C for 30 min in argon, while almost all sodium cyanide decomposes within 30 min in air or O_2 with mass ratio of ferric oxide to sodium cyanide of 1:1. The increase of ferric oxide addition, temperature, and heating time facilitates the destruction of sodium cyanide. It is believed that with ferric oxide addition, NaCN reacts with Fe_2O_3 to form $Na_4Fe(CN)_6$, Na_2CO_3, $NaNO_2$ and Fe_3O_4 in argon. NaCN decomposes into NaCNO, $Na_4Fe(CN)_6$, minor $NaNO_2$, and the formed NaCNO and $Na_4Fe(CN)_6$ further decompose into Na_2CO_3, CO_2, N_2, FeO_x, and minor NO_x in air or O_2.

Key words: cyanide destruction; thermal decomposition; ferric oxide; catalytic oxidation; sodium cyanide

1 Introduction

Cyanide leaching is widely used in gold extraction due to its advantages of maturity, low cost and high leaching rate. Around the world, about 80% of gold is recovered by this method [1,2]. As a result, hundreds of millions of tons of cyanide-containing wastes are produced, which are hazardous to human health and environment [3,4]. Constraints on cyanide (especially the free and weak-acid dissociable cyanides) discharge are being tightened by local governments worldwide due to its high toxicity and volatility [5]. Thus, the disposal of cyanide-containing wastes from the cyanidation process is a great challenge for the gold mining industry. The situation in China is much stricter because cyanide-containing solid wastes have been enclosed in the List of National Hazardous Waste by the central government from 2016 [6]. It is required by law that the cyanide-containing solid wastes must be detoxified to a limit of 5 mg/L total CN before being discharged to tailing ponds [7,8]. Otherwise, a penalty rate of $150 per ton will be imposed in addition to the disposal fee charged by the certified company [9]. Therefore, the research of effective and versatile cyanide destruction technologies has been becoming critical to the sustainable development of the gold mining industry.

Corresponding author: Feng XIE, Tel: +86-24-83672298, E-mail: xief@smm.neu.edu.cn;
Wei WANG, Tel: +86-24-83672298, E-mail: wangwei@smm.neu.edu.cn
DOI: 10.1016/S1003-6326(21)65565-6

Many technologies of destructing cyanide effluent have been reported [10,11]. Nowadays, natural degradation and acidification-volatilization-reneutralization (AVR) processes are seldom used for cyanide effluent treatment due to environmental concerns [10,12,13]. Alkaline chlorination [14] is the predominant mode in the treatment of cyanide-containing wastewater. However, it only works on free or weakly bound cyanide with harsh chemical conditions. Similarly, some other alternative treatments, such as sulfur dioxide [15], ozone [16,17], hydrogen peroxide [18], and iron/copper precipitation processes [19] are also commonly used for cyanide destruction in practice. However, these methods have the problems of high chemical costs, the formation of toxic intermediate and complicated process, which need further improvement [20]. Some eco-friendly process, such as activated carbon adsorption [21,22], natural zeolite adsorption [23], resin ions [24,25], photo-oxidation [26,27], electrolytic oxidation [28,29] and biological methods [30], have been devised to destroy cyanides. However, the complex nature of cyanide wastewater, primarily the high concentrations of cyanide, may seriously restrict their industrial application.

Efficient thermal decomposition or destruction of cyanides in cyanide-containing solid wastes is seldom reported. The organic effluent and exhaust gas produced in the sodium cyanide production process were treated by incineration at high temperatures, and the results showed that the highly toxic organic cyanide decomposed into H_2O and CO_2 [31]. The cyanide slag arising from the sodium cyanide plant was mixed with coal and clay at the mass ratio of 6:4:1 to make pellets, which were then incinerated at about 850 °C in a special furnace. About 94.6% of cyanide was destroyed [32]. However, the mechanism of the destruction of cyanide was less described in the references. The main species of cyanide remaining in cyanide-containing solid wastes are free cyanide and metal-cyanide complexes. About 10%−30% of cyanogen is free cyanide. Ferric oxide is usually used as a catalyst for the decomposition of materials [33,34]. In this study, sodium cyanide was taken as the free cyanide, and the mechanism of the destruction of sodium cyanide by thermal decomposition with ferric oxide addition was examined with the purpose to elucidate the potential use of the thermal decomposition for destructing cyanide-containing solid wastes from gold cyanidation process. The effect of operational parameters on the destruction of sodium cyanide was examined in detail, including Fe_2O_3 addition, temperature, heating time and atmosphere. The mechanism of the catalytic destruction of sodium cyanide by ferric oxide was also discussed.

2 Experimental

2.1 Materials

The industrial-grade solid sodium cyanide used in this study was supplied by a local gold mining company in Inner Mongolia, China. The sodium cyanide was carefully stored in a safe sealed bottle. Before being used as the feed material for this study, it was carefully ground to less than 74 μm in a fume hood. Fe_2O_3 and NaOH were supplied by local chemical manufacture in Shenyang, China and Kermel Co., Ltd. in Tianjin, China, respectively. The purity of O_2 and Ar gases used in this study was more than 99.995%. Distilled water was used throughout the experiments.

2.2 Procedure

About 0.2−0.4 g of the feed was mixed with various predetermined amounts of ferric oxide (0−0.6 g) in a ball mill for 20 min. Then, the mixture was ground and remixed carefully in an agate mortar to ensure the homogeneity. The mixture was loaded in an opening porcelain crucible, which was then heated in a programmable resistance furnace from the room temperature to the setting temperature (100−600 °C) at 10 °C/min in air. After being heated at the set temperature for a set time, the clinker was immediately taken out and cooled in air. The mixture and clinker were weighed and the masses were recorded, respectively. According to DONG et al [35], O_2 played an important role in the decomposition of sodium cyanate, so the destruction of sodium cyanide by thermal decomposition with ferric oxide addition was evaluated in Ar and O_2 atmosphere.

In the case of heating in Ar atmosphere, the experiments were performed in a horizontal tube furnace. The furnace tube was purged with a stream of Ar gas at 150 mL/min for 20 min when the crucible was loaded. Then, the pre-set heating programs were run in Ar gas flowing at 50 mL/min.

When the pre-set heating programs were over, the clinker was moved to the furnace door to cool in dynamic Ar. The gas exiting from the furnace was bubbled through a 15 mL solution of 10 g/L NaOH to absorb CO_2 or NO_x.

In the case of heating in O_2 atmosphere, O_2 was charged into the tube furnace intermittently or continuously as needed. O_2 was charged into the furnace for 2 min each time with a flow rate of 150 mL/min when O_2 was needed intermittently. Other operations in O_2 were consistent with those in Ar.

The mixture and clinker were carefully crushed to below 74 μm in the fume hood with an agate mortar and pestle and then leached with distilled water for 10 min at room temperature. The leached slurry was filtrated and washed with distilled water. The filtrate and wash water were thoroughly mixed and then diluted to 100 mL with distilled water.

2.3 Analysis

The concentration of NaCN and Na_2CO_3 in the filtrate was analyzed according to the methods described in Refs. [36, 37], respectively. The filter residue was analyzed for Fe^{2+} according to AQSIQ [38]. The concentrations of caustic alkali (N_K, in form of Na_2O), carbonate alkali (N_C, in form of Na_2O), and total alkali (N_T, in form of Na_2O) in the NaOH bubbled solution were analyzed by the volumetric method [39]. The content of Na_2CO_3 in the feed was analyzed by the gravimetric method with 5% $BaCl_2$ solution. The remaining solutions were collected in a waste tank for unified treatment. Some representative mixture and clinker were taken to analyze the contents of Na, C, N, NO_2^- and NO_3^- for the balance calculation of elements using atomic absorption spectrometer, carbon−sulfur analyzer, oxygen−nitrogen analyzer, and ion chromatography, respectively.

The characterization of the feed was investigated by a differential scanning calorimetry (DSC) and thermogravimetric (TG) simultaneous thermal analyzer (NETZSCH STA409C/CD) at a heating rate of 10 °C/min under a dynamic Ar or air atmosphere with a flow rate of 50 mL/min. About 6.5 mg of the feed was loaded in an alumina crucible and heated from room temperature to 900 or 1100 °C. Each experiment was performed twice for reproducibility, and exact thermograms were obtained.

The mineral compositions of clinker were estimated using an Ultima IV with Cu K_α radiation. The diffractometry was conducted with a scanning speed of 5 (°)/min from 10 to 80° at 40 kV and 40 mA. Each powder sample was carefully and evenly placed on a rectangular quartz holder, flattened with a glass slide. The data were analyzed by the MDI Jade using the PDF2−2004 database.

2.4 Calculation

In the experiment process, the mixture was oxidized, the mass changed, and the highly toxic NaCN decomposed into non-toxic products. The mass ratio of the clinker to the mixture ($w_{c/m}$) and the residual rate of NaCN to the feed (η_{cy}) are defined as follows to evaluate the mass change of the mixture and the decomposition of NaCN:

$$w_{c/m}=(m_c/m_m)\times 100\% \quad (1)$$

$$\eta_{cy}=(w_{cy}\times m_c)/[1/(1+w_{f/cy})m_m] =[w_{cy}(1+w_{f/cy})w_{c/m}]\times 100\% \quad (2)$$

where m_c is the mass of the clinker; m_m is the mass of the mixture; w_{cy} is the mass ratio of NaCN in the clinker; $w_{f/cy}$ is the mass ratio of ferric oxide to the feed.

3 Results and discussion

3.1 Characterization of feed material

The chemical analysis shows that the feed contains 93.70% NaCN, 0.70% Na_2CO_3, and 3.85% NaCNO. The ferric oxide used in this study contains 99.85% Fe_2O_3. The XRD patterns of the feed and ferric oxide are shown in Fig. 1. The main phase is NaCN (cubic, $Fm\bar{3}m$ (225)) in the feed and Fe_2O_3 (hexagonal, $R\bar{3}c$ (167)) in the ferric oxide.

The TG−DSC curves of the feed in Ar and air atmosphere are shown in Fig. 2(a) and 2(b), respectively. Figure 2(a) shows that the sample mass remains almost constant below 700 °C, and then drops sharply with the increase of temperature. According to the extrapolated onset temperature method, the TG curve shows that the initial decomposition of the feed occurs at 879.2 °C. Two endothermic peaks occur at 491.1 and 557.9 °C on the DSC curve. However, the TG curve shows no mass change at these temperatures, indicating that the sample undergoes a potential phase change

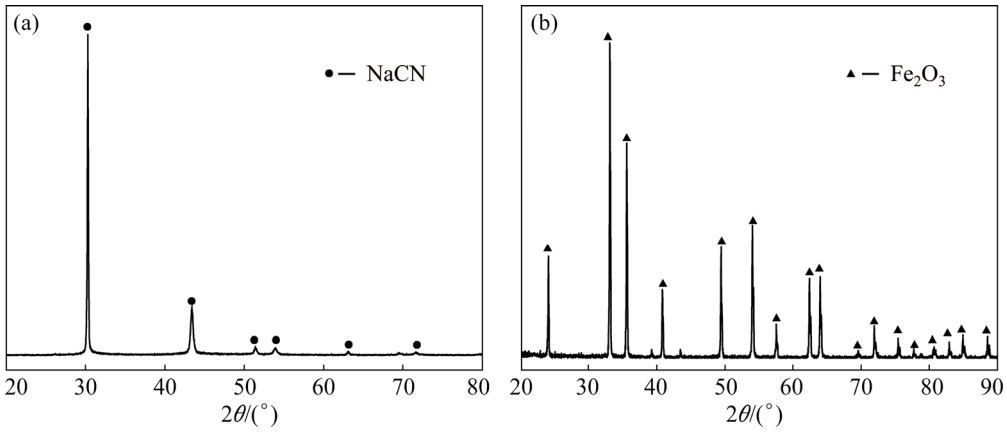

Fig. 1 XRD pattern of feed (a) and ferric oxide (b)

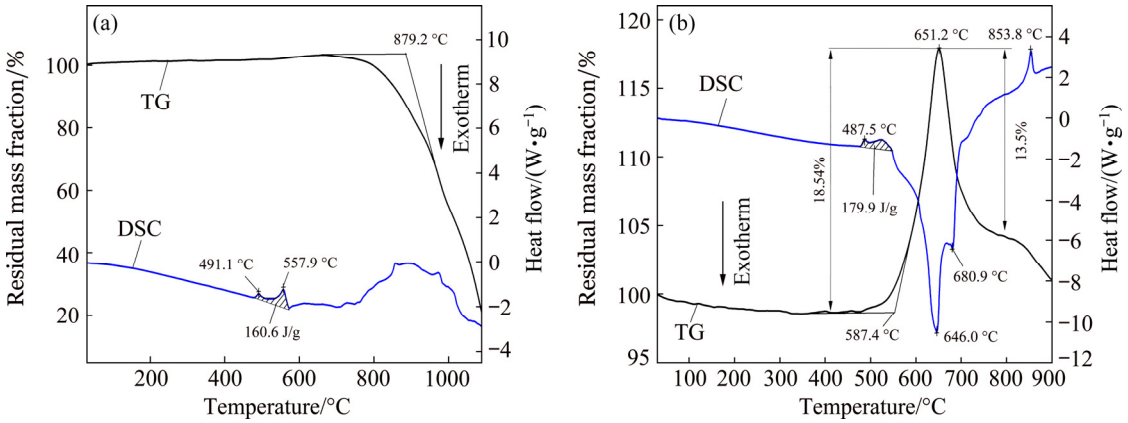

Fig. 2 TG−DSC curves for feed in Ar (a) and in air (b) at heating rate of 10 °C/min

before decomposition. According to the calculation, the endothermic peak area on the DSC curve gives a heat of 160.6 J/g, which is close to the melting enthalpy of 179.4 J/g for NaCN [40]. Because it is reported that the melting point of NaCN is 563 °C [41], the endothermic peak at 557.9 °C is probably caused by the melting of NaCN. A very broad endothermic area occurs between 700 and 1050 °C on the DSC curve. Considering the significant decrease of mass above 700 °C on the TG curve, the endothermic peak is due to the volatilization of NaCN.

Figure 2(b) shows that the sample mass remains almost constant below 450 °C. The sample mass increases by 18.54% between 450 and 651.2 °C while it decreases by 13.58% between 651.2 and 800 °C. This is due to the oxidation of NaCN in air to NaCNO and the decomposition of NaCNO to Na_2CO_3 [42,43]. According to the extrapolated onset temperature method, the initial oxidization of NaCN occurs at 587.4 °C. The DSC curve shows that a broad endothermic peak giving heat of 179.9 J/g occurs around 487.5 °C, which is close to the results of Fig. 2(a). Another two exothermic peaks occur at 646.0 and 680.9 °C due to the oxidation of NaCN and the decomposition of NaCNO. An endothermic peak observed at 853.8 °C on the DSC curve corresponds to the melting of Na_2CO_3 and its volatilization [44,45]. Overall, it is suggested that the decomposition of the NaCN in air happens above 500 °C.

3.2 Destruction of NaCN by thermal decomposition in air

The decomposition of NaCN in air below 350 °C was investigated. The feed was heated in air from room temperature to the pre-set temperature (100−350 °C) at 10 °C/min. Thermal decomposition results are shown in Fig. 3. In Fig. 3, the mass ratio of the clinker to the mixture ($w_{c/m}$) remains almost constant when heated below 350 °C without duration. $w_{c/m}$ increases slightly while the residual rate of NaCN to the feed (η_{cy}) decreases slightly at 350 °C with the prolongation of holding time,

which suggests slight oxidization of the feed. This implies that NaCN hardly decomposes in air even when heated at 350 °C for 60 min.

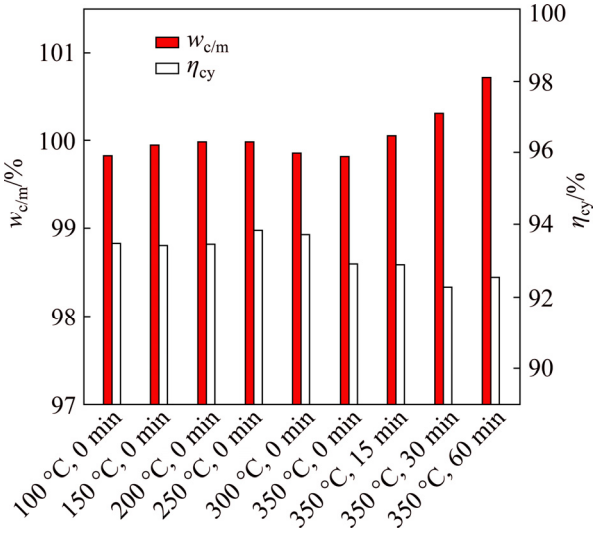

Fig. 3 Variation of mass ratio of clinker to mixture ($w_{c/m}$) and residual rate of NaCN to feed (η_{cy}) with various heating treatments

XRD patterns of the feed heated at 350 °C (Fig. 4) show that the phase in all clinker is NaCN with similar peak intensities. When 2θ=41.3° and 46.0°, two unidentified peaks occur in the clinker heated at 350 °C for 60 min. Therefore, NaCN is considered to poorly decompose below 350 °C.

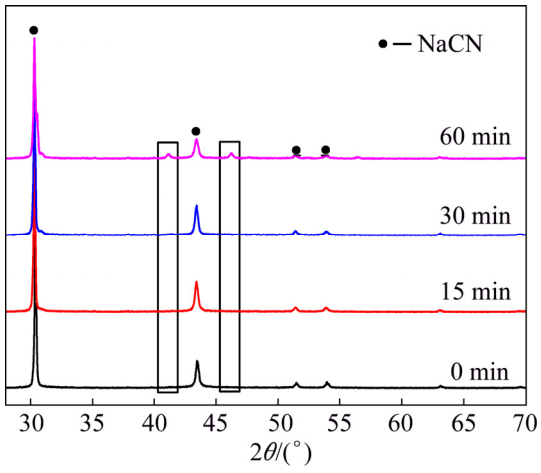

Fig. 4 XRD patterns of feed heated at 350 °C for different time in air

3.3 Effect of Fe_2O_3 on destruction of NaCN in Ar

The effect of Fe_2O_3 on the destruction of NaCN by thermal decomposition was investigated with the mass ratio of ferric oxide to the feed ($w_{f/cy}$) varied between 0:1 and 18:1 at 350 °C for 30 min in Ar. The clinker in all cases is dark-red powder with magneticity, suggesting that Fe_3O_4 is formed in the clinker. The thermal decomposition results presented in Fig. 5 show that the mass change of the samples is negligible in all cases. η_{cy} decreases as $w_{f/cy}$ increases from 0:1 to 18:1, indicating that NaCN decomposes under the experimental conditions and Fe_2O_3 promotes the destruction of NaCN. The composition of the clinker heated at $w_{f/cy}$ of 1:1 and 4.5:1 (Fig. 6) shows that NO_2^-, Fe^{2+} and Na_2CO_3 are found in the clinker, but NO_3^- is not found, suggesting that NaCN reacts with Fe_2O_3 to form $NaNO_2$, Fe_3O_4, and Na_2CO_3.

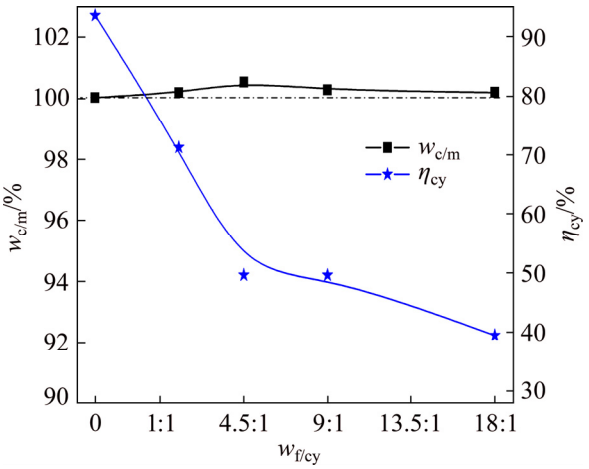

Fig. 5 Variation of mass ratio of clinker to mixture ($w_{c/m}$) and residual rate of NaCN to feed (η_{cy}) with mass ratio of ferric oxide to feed ($w_{f/cy}$) varied from 0:1 to 18:1

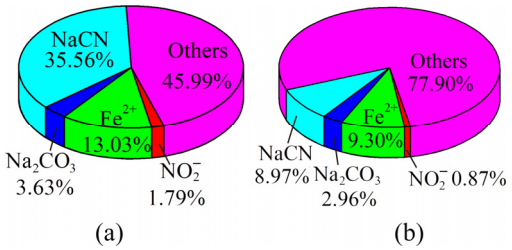

Fig. 6 Main compositions of clinker heated at mass ratio of ferric oxide to feed ($w_{f/cy}$) of 0:1 (a) and 4.5:1 (b)

XRD patterns of the clinker (Fig. 7) show that the clinker is made of NaCN, Fe_2O_3, Fe_3O_4 and $Na_4Fe(CN)_6$. $NaNO_2$ and Na_2CO_3 are not observed on XRD patterns due to their low content in the clinker. The formation of Fe_3O_4 results in the clinker being magnetic. The diffraction peak intensity of NaCN, Fe_3O_4, and $Na_4Fe(CN)_6$ decreases with the increase of Fe_2O_3 due to the decrease of the mass ratio of these components.

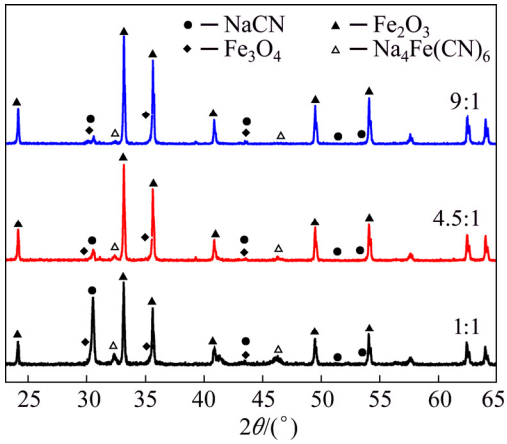

Fig. 7 XRD patterns of clinker heated at different mass ratios of ferric oxide to feed ($w_{f/cy}$)

The content of the bubbled NaOH solution is given in Table 1. Compared with the blank solution, the contents of the bubbled solution change little, suggesting that no gas that could be absorbed by NaOH was formed when the samples were heated in Ar. Overall, the destruction of NaCN by thermal decomposition with Fe_2O_3 addition in Ar can be described by

$$11Fe_2O_3+7NaCN\rightarrow 7Fe_3O_4+Na_4Fe(CN)_6+Na_2CO_3+NaNO_2 \quad (3)$$

3.4 Effect of Fe_2O_3 on destruction of NaCN in air

3.4.1 Fe_2O_3 addition

The effect of Fe_2O_3 on the destruction of NaCN by thermal decomposition in air was investigated at 350 °C for 30 min. $w_{f/cy}$ was varied from 0.01:1 to 1.5:1. The macrostructures of the clinker with various $w_{f/cy}$ are shown in Fig. 8. It can be seen that the clinker sintered together in all cases, and it melted when $w_{f/cy}$ is 0.3:1 and 0.5:1. As $w_{f/cy}$ increases, the color of the clinker changes from light-red to yellow, to black, and then to red, indicating that NaCN reacts with Fe_2O_3 when the samples are heated in air.

Table 1 Contents of bubbled NaOH solution

No.	$w_{f/cy}$	N_K/(g·L^{-1})	N_C/(g·L^{-1})	N_T/(g·L^{-1})	NO_2^-/(mg·L^{-1})	NO_3^-/(mg·L^{-1})
1	1:1	7.29	0.90	8.19	8.06	<0.001
2	4.5:1	7.29	0.90	8.19	7.67	<0.001
3	9:1	7.21	0.98	8.19	–	–
4	18:1	7.30	0.88	8.19	–	–
5	Blank	7.32	0.87	8.19	7.90	<0.001

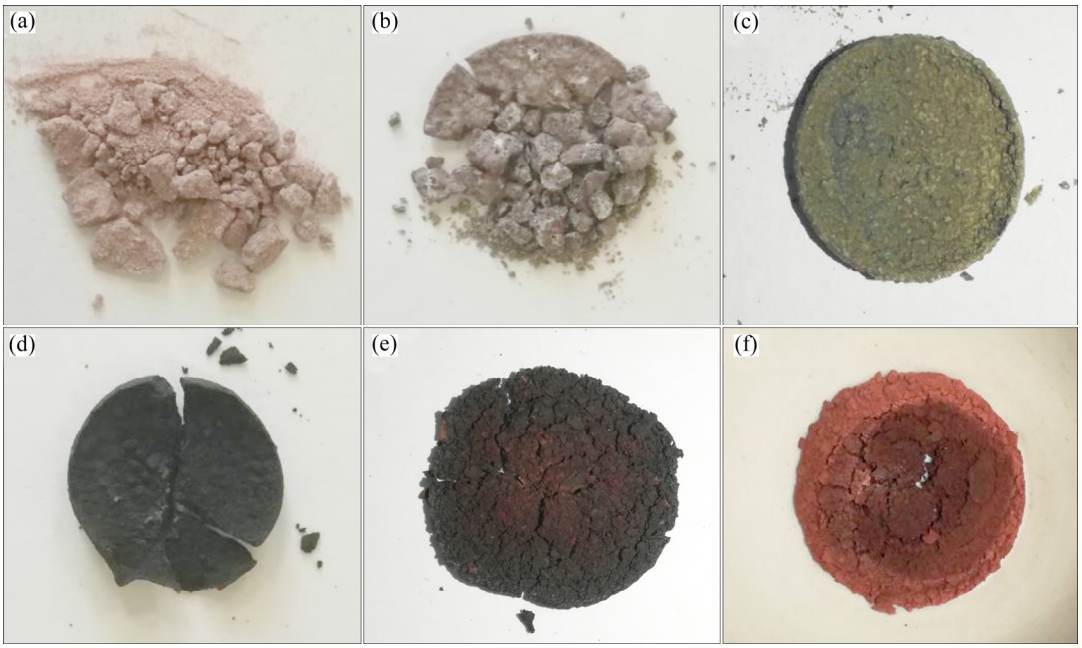

Fig. 8 Macrostructures of clinker with different mass ratios of ferric oxide to feed ($w_{f/cy}$): (a) 0.01:1; (b) 0.1:1; (c) 0.3:1; (d) 0.5:1; (e) 0.7:1; (f) 1:1

The thermal decomposition results in Fig. 9 show that $w_{c/m}$ is more than 100% in all cases. It increases rapidly when $w_{f/cy}$ increases to 0.3:1, remains almost constant when $w_{f/cy}$ is between 0.3:1 and 1:1, and then decreases with further increase of $w_{f/cy}$. η_{cy} decreases sharply when $w_{f/cy}$ increases to 0.6:1. When $w_{f/cy}$ is more than 0.6:1, η_{cy} decreases to nearly zero. The mass fraction of Na_2CO_3 increases with the increase of $w_{f/cy}$. This suggests that more Fe_2O_3 promotes the destruction of NaCN and the formation of Na_2CO_3 in air.

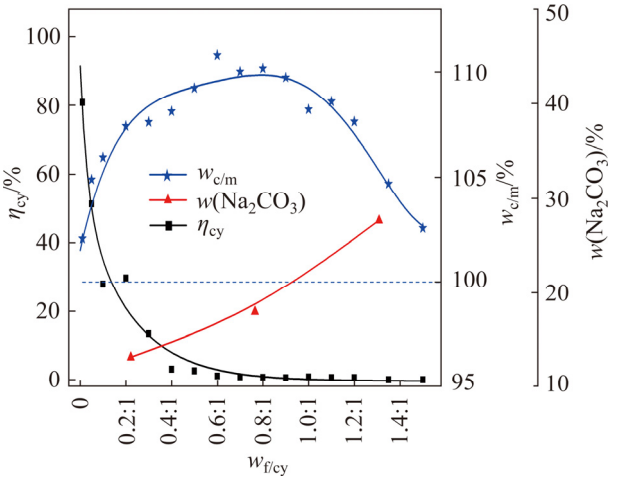

Fig. 9 Variation of mass ratio of clinker to mixture ($w_{c/m}$), mass fraction of Na_2CO_3 in clinker and residual rate of NaCN to feed (η_{cy}) with mass ratio of ferric oxide to feed ($w_{f/cy}$) varied from 0.01:1 to 1.5:1

XRD patterns of the clinker (Fig. 10) show that the phase composition of the clinker varies greatly. In Fig. 10(a), the clinker is made of NaCN, NaCNO and Fe_2O_3 at $w_{f/cy}$ of 0.01:1, suggesting that part of NaCN decomposes into NaCNO. The new phase of Na_2CO_3 is observed at $w_{f/cy}$ of 0.05:1 and 0.1:1. The clinker is composed of NaCN, NaCNO, Na_2CO_3, $Na_4Fe(CN)_6$ and $Na_2O{\cdot}Fe_2O_3$ when $w_{f/cy}$ is 0.2:1 and 0.3:1. The diffraction peak intensity of NaCN decreases rapidly, while that of NaCNO first increases and then decreases. The diffraction peak intensity of $Na_4Fe(CN)_6$ increases, and that of Fe_2O_3 first increases and then disappears. According to the previous research [35], it is considered that NaCN is oxidized to NaCNO by Reaction (4), NaCNO decomposes to Na_2CO_3 by Reactions (5) and (6), and Fe_2O_3 reacts with NaCN and Na_2CO_3 to form $Na_4Fe(CN)_6$ and $Na_2O{\cdot}Fe_2O_3$ by Reactions (3) and (7), respectively.

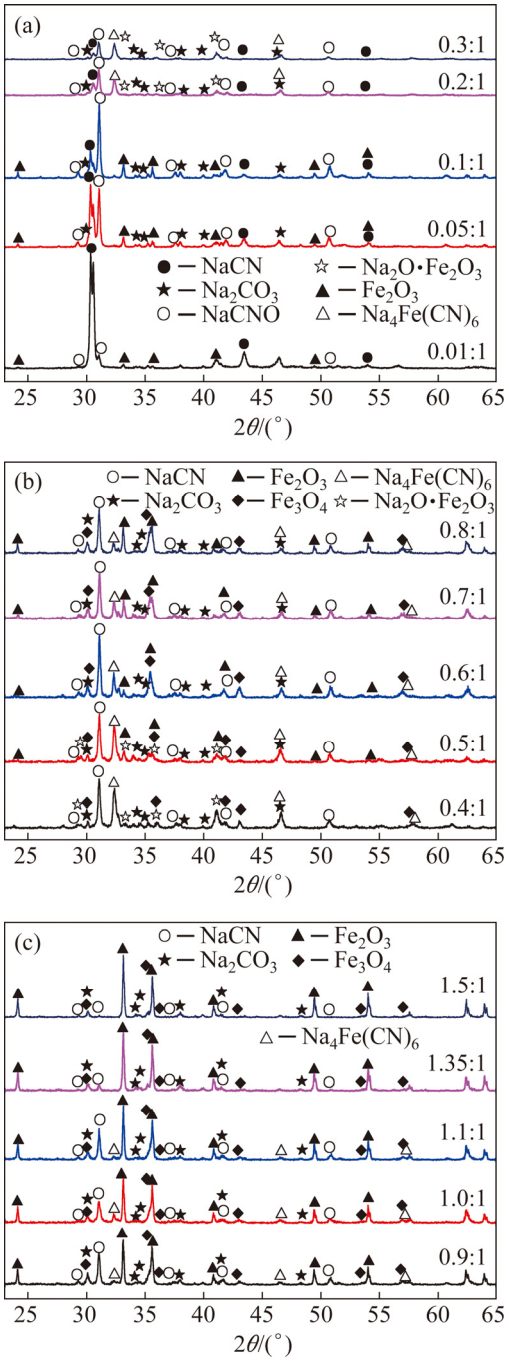

Fig. 10 XRD patterns of clinker with varied mass ratio of ferric oxide to feed ($w_{f/cy}$): (a) 0.01:1−0.3:1; (b) 0.4:1−0.8:1; (c) 0.9:1−1.5:1

$$NaCN+O_2 \xrightarrow{Fe_2O_3} NaCNO \quad (4)$$

$$NaCNO+O_2 \xrightarrow{Fe_2O_3} Na_2CO_3+N_2\uparrow+CO_2\uparrow \quad (5)$$

$$NaCNO+O_2 \xrightarrow{Fe_2O_3} Na_2CO_3+CO_2\uparrow+NO_x\uparrow \quad (6)$$

$$Na_2CO_3+Fe_2O_3 \rightarrow Na_2O\cdot Fe_2O_3+CO_2\uparrow \quad (7)$$

In Figs. 10(b, c), the diffraction peak of NaCN disappears while that of Fe_3O_4 appears at $w_{f/cy}$ of

0.4:1, indicating that NaCN reacts with Fe_2O_3 to form Fe_3O_4. Fe_2O_3 occurs again when $w_{f/cy}$ is more than 0.5:1, at which the clinker consists of NaCNO, Na_2CO_3, $Na_4Fe(CN)_6$, $Na_2O{\cdot}Fe_2O_3$, Fe_3O_4 and Fe_2O_3. When $w_{f/cy}$ is varied between 0.6:1 and 1.1:1, the clinker is made of NaCNO, Na_2CO_3, $Na_4Fe(CN)_6$, Fe_3O_4 and Fe_2O_3. The diffraction peak of $Na_4Fe(CN)_6$ disappears when $w_{f/cy}$ is above 1.1:1, suggesting that $Na_4Fe(CN)_6$ decomposes with the increase of Fe_2O_3 addition, and Fe_2O_3 also promotes the decomposition of $Na_4Fe(CN)_6$. The diffraction peak intensity of NaCNO first increases and then decreases, suggesting that more Fe_2O_3 favors the oxidization of NaCN and the decomposition of NaCNO. When $w_{f/cy}$ is 1.35:1 and 1.5:1, the diffraction peak of NaCNO almost disappears, indicating that NaCNO decomposes almost completely. The diffraction peak of $Na_2O{\cdot}Fe_2O_3$ appears at $w_{f/cy}$ of 0.2:1−0.5:1. According to the macrostructures of the clinker, it is considered that Na_2CO_3 reacts with Fe_2O_3 in the melt.

3.4.2 Heating temperature

The effect of temperature on the destruction of NaCN by ferric oxide was studied at 100−600 °C without duration with $w_{f/cy}$ of 1:1. The thermal decomposition results (Fig. 11) show that $w_{c/m}$ is more than 100% in all cases. It remains almost constant below 200 °C, rises rapidly at 200−400 °C, and then drops significantly above 400 °C, indicating that NaCN decomposes better at higher temperatures. The mass fraction of Na_2CO_3 increases slowly below 450 °C, and increases rapidly above 450 °C, indicating that the higher temperatures favor the formation of Na_2CO_3. η_{cy} remains almost constant below 200 °C, decreases sharply between 200 and 300 °C, and gradually decreases to near zero above 300 °C. This suggests that higher temperatures promote the destruction of NaCN.

The phase composition of the clinker heated at various temperatures is revealed by XRD (Fig. 12), showing that the phase composition of the clinker varies greatly. Only NaCN and Fe_2O_3 are observed at 200 °C, suggesting that NaCN decomposes hardly at this temperature. NaCNO appears when the temperature increases to 250 °C, suggesting that Reaction (4) happens at 250 °C. The clinker heated at 300 and 350 °C is made of NaCNO, Na_2CO_3, $Na_4Fe(CN)_6$, Fe_3O_4 and Fe_2O_3. NaCN is absent. This suggests that almost all NaCN decomposes to NaCNO, Na_2CO_3 and $Na_4Fe(CN)_6$. Between 200 and 300 °C, the diffraction peak intensity of NaCN decreases to disappear whilst that of NaCNO increases correspondingly, suggesting that NaCN is oxidized to NaCNO. The diffraction peak of $Na_4Fe(CN)_6$ disappears above 400 °C, indicating that it is formed as an intermediate and decomposes at 300−400 °C. The diffraction peak intensity of NaCNO remains almost constant at 300−400 °C, but decreases above 400 °C, implying that NaCNO decomposes at 300−400 °C and decomposes faster above 400 °C. The diffraction peak intensity of Na_2CO_3 increases with the increase of temperature, which is consistent with the results in Fig. 11. Fe_2O_3 has similar diffraction peak intensity in all cases while Fe_3O_4 slightly increases in diffraction peak intensity.

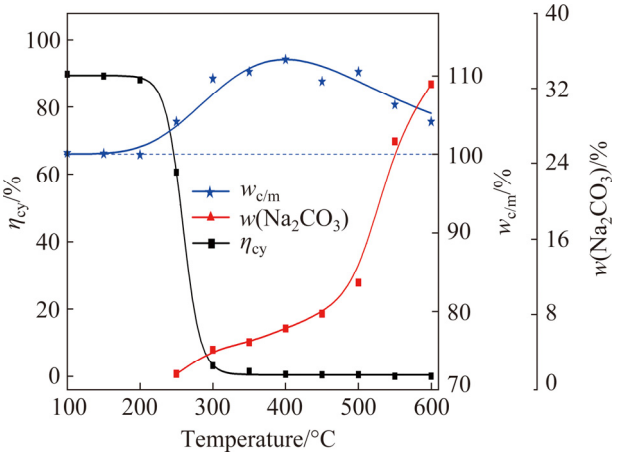

Fig. 11 Variation of mass ratio of clinker to mixture ($w_{c/m}$), mass fraction of Na_2CO_3 in clinker and residual rate of NaCN to feed (η_{cy}) versus temperature without duration

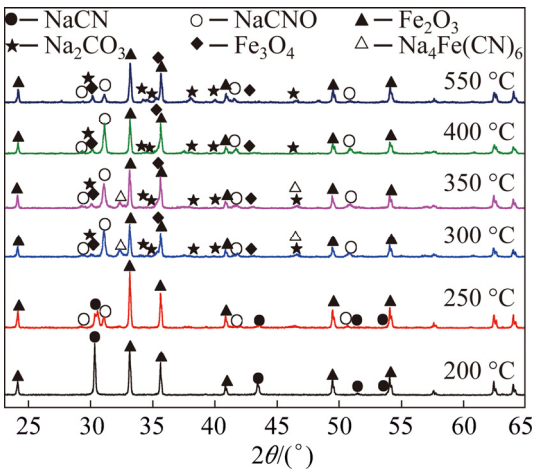

Fig. 12 XRD patterns of clinker heated at 200−550 °C without duration

3.4.3 Heating time

More than 90% of NaCN decomposed above 300 °C without duration at $w_{f/cy}$ of 1:1. Therefore, temperature of 300−400 °C was selected to study the effect of heating time on the destruction of NaCN by ferric oxide. The heating time was varied between 0 and 120 min at 300, 350 and 400 °C and $w_{f/cy}$ of 1:1. The thermal decomposition results are shown in Fig. 13. In Fig. 13(a), $w_{c/m}$ is more than 100% in all cases, and it decreases with the prolongation of heating time. The higher the temperature is, the faster the $w_{c/m}$ decreases. This suggests that higher temperatures and longer time favor the decomposition of the samples.

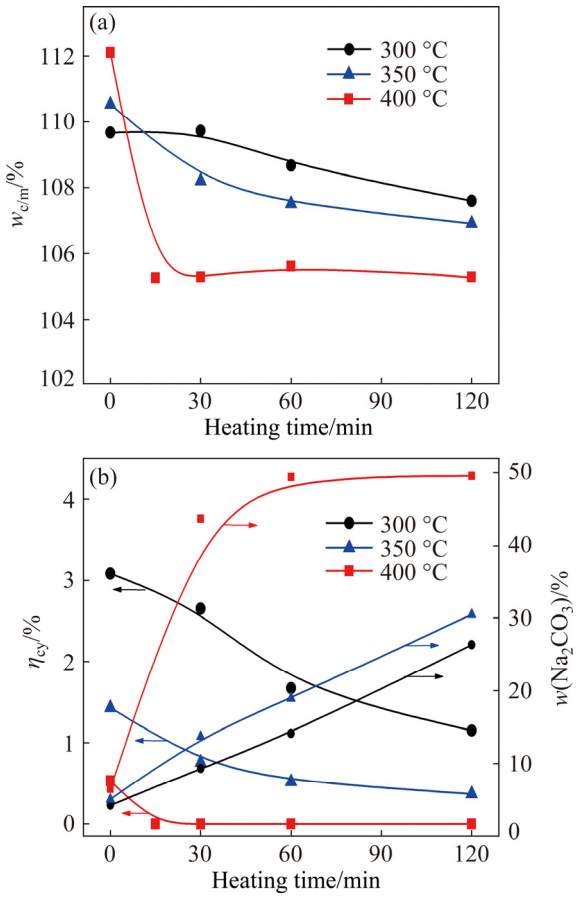

Fig. 13 Variation of mass ratio of clinker to mixture ($w_{c/m}$) (a), and mass fraction of Na_2CO_3 in clinker and residual rate of NaCN to feed (η_{cy}) (b) versus heating time

In Fig. 13(b), the mass fraction of Na_2CO_3 in the clinker increases with the increase of heating time or temperature. The content of Na_2CO_3 is linearly related to the heating time at 300 and 350 °C, and it increases rapidly first and then remains almost constant at 400 °C. This suggests that Na_2CO_3 is gradually formed with the prolongation of heating time at 300 and 350 °C, and the formation of Na_2CO_3 is almost completed within 60 min at 400 °C. η_{cy} decreases with the prolongation of heating time, and the higher temperature is, the less the η_{cy} is, indicating that NaCN decomposes with the increase of heating time, and higher temperatures promote the destruction of NaCN thoroughly.

The chemical composition of the mixture and clinker (Fig. 14) shows that about 85% of C and N remain in the clinker at 400 °C without duration, while about 50% C and almost all N are lost at 400 °C for 30 min. In both cases, the mass change of Na is negligible. Overall, this implies that about 50% C and almost all N run out of the samples in the form of gases.

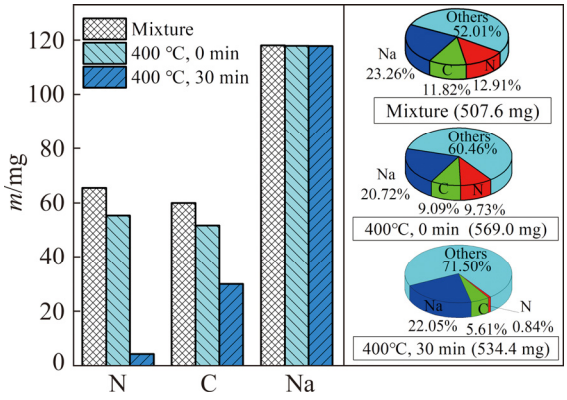

Fig. 14 Compositions of mixture and clinker heated at 400 °C for 0−30 min

The clinker heated at 300, 350, and 400 °C for 0−120 min was analyzed by XRD (Fig. 15). Figures 15(a, b) show that the clinker heated at 300 °C and 350 °C is made of NaCNO, Na_2CO_3, $Na_4Fe(CN)_6$, Fe_2O_3 and Fe_3O_4. The diffraction peak intensity of NaCNO and $Na_4Fe(CN)_6$ decreases with heating time, suggesting that NaCNO and $Na_4Fe(CN)_6$ decompose with the prolongation of heating time. The diffraction peak intensity of Na_2CO_3 increases with heating time, which is consistent with the results in Fig. 13(b). This implies that NaCNO and $Na_4Fe(CN)_6$ decompose into Na_2CO_3. The diffraction peak intensity of Fe_2O_3 and Fe_3O_4 remains almost constant. Figure 15(c) shows that the clinker heated at 400 °C is composed of NaCNO, Na_2CO_3, Fe_2O_3, and Fe_3O_4. The diffraction peak of $Na_4Fe(CN)_6$ disappears, suggesting that $Na_4Fe(CN)_6$ decomposes almost

completely at 400 °C. The diffraction peak of NaCNO decreases to disappear, indicating that NaCNO decomposes rapidly with the prolongation of heating time.

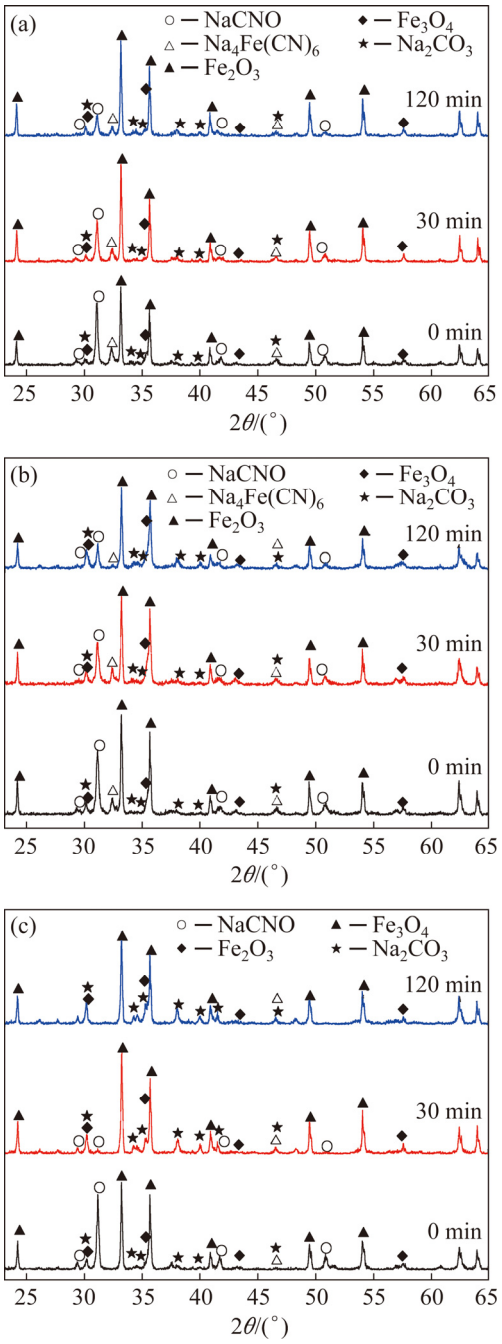

Fig. 15 XRD patterns of clinker heated in air for 0−120 min with mass ratio of ferric oxide to feed ($w_{f/cy}$) of 1:1 at different temperatures: (a) 300 °C; (b) 350 °C; (c) 400 °C

3.5 Effect of Fe_2O_3 on destruction of NaCN in O_2

Subsections 3.3 and 3.4 show that O_2 has a serious impact on the destruction of NaCN. Hence, different feeding amounts of O_2 were selected for studying the destruction of NaCN by ferric oxide at 350 °C for 30 min. The macrostructure of the clinker is shown in Fig. 16. It can be seen that more clinker melts with more O_2, and the molten clinker is black but strongly magnetic. This implies that more O_2 favors the clinker melting and the reaction of NaCN with Fe_2O_3. The content of the bubbled NaOH solution (Table 2) shows that as the feeding amount of O_2 increases, the concentration of N_K decreases while the concentration of N_C increases. This suggests that more CO_2 is formed as the feeding amount of O_2 increases. New NO_2^- is found in the bubbled solution, indicating that a small amount of NO_x is formed in the destruction of NaCN [46].

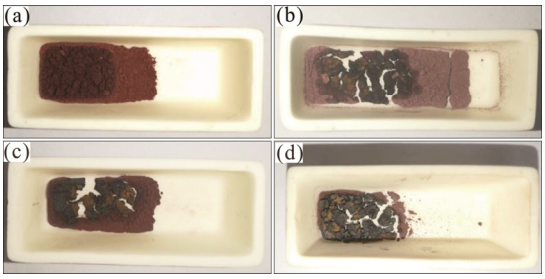

Fig. 16 Macrostructures of clinker with different feeding amounts of O_2 at flow rate of 150 mL/min: (a) 2-times; (b) 4-times; (c) 8-times; (d) Continuously

The thermal decomposition results presented in Fig. 17 show that $w_{c/m}$ is more than 100% in all cases. It remains almost constant when O_2 is fed into the furnace intermittently, but it decreases when O_2 is fed continuously. η_{cy} decreases with the increase of feeding amount of O_2, suggesting that more O_2 promotes the destruction of NaCN. The mass fractions of Na_2CO_3 and Fe^{2+} increase, suggesting that more O_2 promotes the reaction between NaCN and Fe_2O_3, forming more Na_2CO_3 and Fe_3O_4 [47].

The composition of the mixture and clinker with intermittent and continuous O_2 feeding (Fig. 18) shows that about 60% N and 85%−90% C remain in the clinker heated in O_2. New NO_2^- is found in the clinker, but NO_3^- is not, suggesting that a small amount of NaCN decomposes to $NaNO_2$ during the thermal decomposition process. The amount of C and Na in the mixture is almost equal to that in the clinker and exhaust gas. Compared with the results in Table 2, CO_2, N_2 and minor NO_x are formed in the destruction of NaCN [42,48].

Table 2 Contents of decomposition exhaust gas bubbled solution

No.	N_K/(g·L^{-1})	N_C/(g·L^{-1})	N_T/(g·L^{-1})	NO_3^-/(mg·L^{-1})	NO_2^-/(mg·L^{-1})	O_2 feeding amount
1	6.49	1.83	8.33	–	–	Intermittent, 2-times
2	6.21	2.12	8.33	–	–	Intermittent, 4-times
3	5.94	2.39	8.33	<0.001	36.23	Intermittent, 8-times
4	4.83	3.45	8.29	<0.001	23.72	Continuous
5	7.52	0.75	8.27	<0.001	2.16	Blank

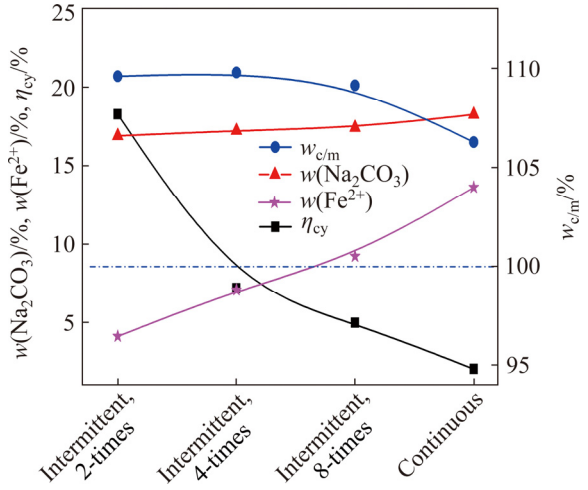

Fig. 17 Variation of mass ratio of clinker to mixture ($w_{c/m}$), mass fraction of Na_2CO_3 and Fe^{2+} in clinker and residual rate of NaCN to feed (η_{cy}) with feeding amounts of O_2

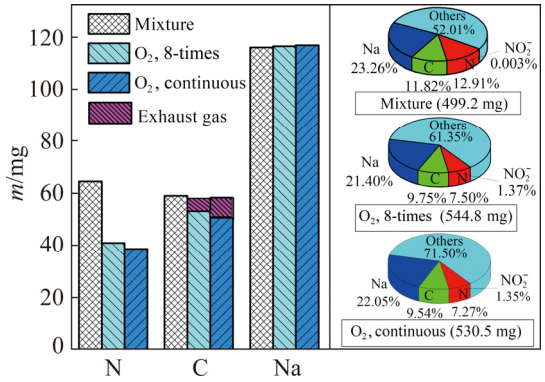

Fig. 18 Main compositions of mixture and clinker with intermittent and continuous O_2 feeding

The phase composition of the clinker with different feeding amounts of O_2 was analyzed by XRD (Fig. 19). It is shown that the clinker heated in O_2 is comprised of NaCNO, Fe_3O_4, Na_2CO_3 and $Na_4Fe(CN)_6$. As the feeding amount of O_2 increases, the diffraction peak of NaCN is gradually fade away, and the diffraction peak intensity of Fe_2O_3 decreases while that of Fe_3O_4 and $Na_4Fe(CN)_6$ increase, suggesting that the more O_2 promotes Reaction (3). The diffraction peak intensity of

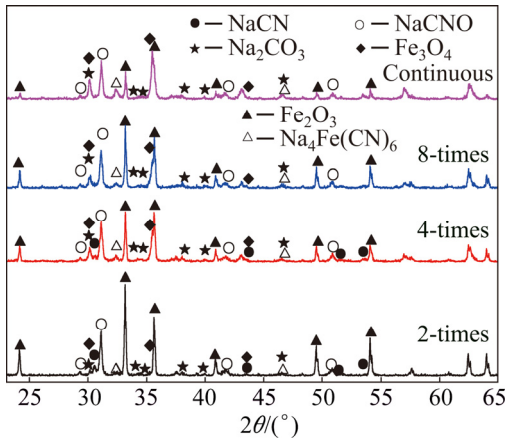

Fig. 19 XRD patterns of clinker with different feeding amounts of O_2

Na_2CO_3 is enhanced while that of NaCNO remains almost constant. According to the previous research [35], more O_2 helps Reaction (4) and part of NaCNO and $Na_4Fe(CN)_6$ decomposes by Reactions (5) and (6), and Reactions (8) and (9), respectively, under these conditions:

$$Na_4Fe(CN)_6 + O_2 \rightarrow Na_2CO_3 + N_2\uparrow + CO_2\uparrow + FeO_x \quad (8)$$

$$Na_4Fe(CN)_6 + O_2 \rightarrow Na_2CO_3 + NO_x\uparrow + CO_2\uparrow + FeO_x \quad (9)$$

4 Conclusions

(1) NaCN does not decompose below 587.4 °C in air or below 879.2 °C in Ar.

(2) In the presence of Fe_2O_3, about 60% NaCN decomposes at 350 °C for 30 min in Ar while almost all NaCN decomposes at 350 °C and $w_{f/cy}$ of 1:1 for 30 min in air or O_2.

(3) The increase of Fe_2O_3 addition and temperature can result in the completed destruction of NaCN within 30 min. The optimal parameters for the destruction of NaCN by thermal decomposition are to heat the mixture in air above 350 °C for 30 min with $w_{f/cy}$ more than 1:1.

(4) The catalytic oxidation of cyanide by Fe_2O_3 addition is believed to follow a series of reactions: NaCN reacts with Fe_2O_3 to form $Na_4Fe(CN)_6$, Na_2CO_3, $NaNO_2$ and Fe_3O_4 in Ar. When the mixture is heated in air or O_2, NaCN decomposes into NaCNO, $Na_4Fe(CN)_6$, Na_2CO_3 and minor $NaNO_2$. The formed NaCNO and $Na_4Fe(CN)_6$ further decompose into Na_2CO_3, CO_2, N_2, FeO_x and minor NO_x.

Acknowledgments

The authors are grateful for the financial supports from the National Key R&D Program of China (2018YFC0604604), the National Natural Science Foundation of China−Yunnan Joint Fund (U1702252), the Fundamental Research Funds for Central Universities of China (N182506003), and the Key Scientific Research Project of Liaoning Province, China (2019JH2/10300051). The authors gratefully acknowledge the Analytical and Testing Center, Northeastern University for support in instrumental/data analysis.

References

[1] SEVKET A. Process development metallurgical studies for gold cyanidation process [J]. Minerals and Metallurgical Processing, 2016, 33: 161−171.

[2] XIE Feng, DREISINGER D B. Use of ferricyanide for gold and silver cyanidation [J]. Transactions of Nonferrous Metals Society of China, 2009, 19: 714−718.

[3] LV C C, DING J, QIAN P, LI Q C, YE S F, CHEN Y F. Comprehensive recovery of metals from cyanidation tailing [J]. Minerals Engineering, 2015, 70: 141−147.

[4] ZHANG Ya-li, LI Huai-mei, YU Xian-jin. Fe extraction from high-silicon and aluminum cyanide tailings by pretreatment of water leaching before magnetic separation [J]. Transactions of Nonferrous Metals Society of China, 2013, 23: 1165−1173.

[5] CAMPANELLA B, BIANCALANA L, D'ULIVO L, ONOR M, BRAMANTI E, MESTER Z, PAGLIANO E. Determination of total cyanide in soil by isotope dilution GC/MS following pentafluorobenzyl derivatization [J]. Analytica Chimica Acta, 2017, 961: 74−81.

[6] TU Yu-bo, HAN Pei-wei, WEI Lian-qi, ZHANG Xiao-meng, YU Bo, QIAN Peng, YE Shu-feng. Removal of cyanide adsorbed on pyrite by H_2O_2 oxidation under alkaline conditions [J]. Journal of Environmental Sciences, 2019, 78: 287−292.

[7] GB 18598—2001. Standard for pollution control on the security landfill site for hazardous wastes [S]. (in Chinese)

[8] HJ 943—2018. Technical specification for pollution control of cyanide leaching residue in gold industry [S]. (in Chinese)

[9] Standing Committee of the National People's Congress. Environmental Protection Tax Law of the People's Republic of China [Revised] [Z]. 2016. (in Chinese)

[10] KUYUCAK N, AKCIL A. Cyanide and removal options from effluents in gold mining and metallurgical processes [J]. Minerals Engineering, 2013, 50−51: 13−29.

[11] PIRMORADI M, HASHEMIAN S, SHAYESTEH M R. Kinetics and thermodynamics of cyanide removal by ZnO@NiO nanocrystals [J]. Transactions of Nonferrous Metals Society of China, 2017, 27: 1394−1403.

[12] BRÜGER A, G FAFILEK, RESTREPO B O, LUCAS R M. On the volatilisation and decomposition of cyanide contaminations from gold mining [J]. Science of the Total Environment, 2018, 627: 1167−1173.

[13] TRAN Q B, LOHITNAVY M, PHENRAT T. Assessing potential hydrogen cyanide exposure from cyanide-contaminated mine tailing management practices in Thailand's gold mining [J]. Journal of Environmental Management, 2019, 249: 109357.

[14] EDEN G E, HAMPSON B L, WHEATLAND A B. Destruction of cyanide in waste waters by chlorination [J]. Journal of Chemical Technology and Biotechnology, 2010, 69: 244−249.

[15] ROBBINS G H. Historical development of the INCO SO_2/AIR cyanide destruction process [J]. Cim Bulletin, 1996, 89: 63−69.

[16] YILDIZ E, VAPUR H, GÜL S, BAYAT O. Gradual cyanide treatment using AVR and ozone/UV systems with various catalysts in silver mill effluents [J]. Mineral Processing and Extractive Metallurgy Review, 2013, 114: 115−120.

[17] RYSKIE S, GONZALEZ-MERCHAN C, NECULITA C M, GENTY T. Efficiency of ozone microbubbles for ammonia removal from mine effluents [J]. Minerals Engineering, 2020, 145: 1−8.

[18] YEDDOU A R, CHERGUI S, CHERGUI A, HALET F, HAMZA A, NADJEMI B, OULD-DRIS A, BELKOUCH J. Removal of cyanide in aqueous solution by oxidation with hydrogen peroxide in presence of copper-impregnated activated carbon [J]. Minerals Engineering, 2010, 24: 788−793.

[19] SHARMA V K, RIVERA W, SMITH J O, ÓBRIEN B. Ferrate(VI) oxidation of aqueous cyanide [J]. Environmental Science and Technology, 1998, 32: 2608−2613.

[20] BAHRAMI A, KAZEMI F, ALIGHARDASHI A, GHORBANI Y, ABDOLLAHI M, PARVIZIAN A. Isolation and removal of cyanide from tailing dams in gold processing plant using natural bitumen [J]. Journal of Environmental Management, 2020, 262: 110286.

[21] DEPCI T. Comparison of activated carbon and iron impregnated activated carbon derived from Gölbaşı lignite to remove cyanide from water [J]. Chemical Engineering Journal, 2012, 181−182: 467−478.

[22] DE LA T E, LOZADA A B, ADATTY M, GÁMEZ S. Activated carbon-spinels composites for waste water treatment [J]. Metals, 2018, 8: 1070.

[23] BEYRAGH A, VARSEI M, MESHKINI M, KHODADADI DARBAN A, GHOLAMI E. Kinetic and adsorption isotherms study of cyanide removal from gold processing wastewater using natural and impregnated zeolites [J]. Iranian Journal of Chemistry and Chemical Engineering, 2018, 37: 139−149.

[24] XIE Feng, WANG Wei. Recovery of copper and cyanide from waste cyanide solutions using emulsion liquid membrane with LIX 7950 as the carrier [J]. Environmental Technology, 2017, 38: 1961−1968.

[25] XIE Feng, DREISINGER D B. Copper solvent extraction from alkaline cyanide solution with guanidine extractant LIX 7950 [J]. Transactions of Nonferrous Metals Society of China, 2010, 20: 1136−1140.

[26] BARAKAT M A, CHEN Y T, HUANG C P. Removal of toxic cyanide and Cu(II) Ions from water by illuminated TiO_2 catalyst [J]. Applied Catalysis B−Environmental, 2004, 53: 13−20.

[27] OZCAN E, GOK Z, YEL E. Photo/photochemical oxidation of cyanide and metal−cyanide complexes: Ultraviolet A versus ultraviolet C [J]. Environmental Technology, 2012, 33: 1913−1925.

[28] PÉREZ T, ROSA L L, NAVA J L, LAZARO I, VELASCO G, CRUZ R, RODRIGUEZ I. Electrochemical oxidation of cyanide on 3D Ti–RuO_2 anode using a filter-press electrolyzer [J]. Chemosphere, 2017, 177: 1−6.

[29] ZENG Fei-hu, CHEN Cong, HUANG Xian-feng. Enhanced electro-generated ferrate using Fe(0)-plated carbon sheet as an anode and its online utilization for removal of cyanide [J]. Chemosphere, 2020, 241: 125124.

[30] LI Qing-yun, LU Hui, YIN Ye-xing, QIN Yi-ming, TANG Ai-xing, LIU Hai-bo, LIU You-yan. Synergic effect of adsorption and biodegradation enhance cyanide removal by immobilized *Alcaligenes* sp. strain DN25 [J]. Journal of Hazardous Materials, 2019, 364: 367−375.

[31] LIU Dan, YU Peng-qing. Application of incineration treatment method for wastewater and waste gas in sodium cyanide production process [C]// The 13th National Conference on Water Treatment Chemistry and the Symposium on Water Treatment Chemistry across the Taiwan Straits. Nanjing, China: The Applied Chemistry Academic Committee of Chinese Chemical Society, 2016, 85. (in Chinese)

[32] GUO Qian-jin. Discussion on treatment technology of cyanide waste in sodium cyanide plant [J]. Journal of Shanxi Coal-Mining Administrators College, 2004, 87−88. (in Chinese)

[33] VERÓNICA P N, EMILIO R, MARTA P, ANGELES SANROMAN M. Current advances and trends in electro-Fenton process using heterogeneous catalysts−A review [J]. Chemosphere, 2018, 201: 399−416.

[34] ANTHEA MARIKA G D, CHRISTIAN LAURENCE E A, MARY DONNABELLE L B. Photo-Fenton degradation of methyl orange using hematite (α-Fe_2O_3) of various morphologies [J]. Materials Today: Proceedings, 2020, 22: 248−254.

[35] DONG Kai-wei, XIE Feng, CHANG Yong-feng, CHEN Chun-lin, WANG Wei, LU Dian-kun, GU Xiao-wei. A novel strategy for the efficient decomposition of toxic sodium cyanate by hematite [J]. Chemosphere, 2020, 256: 127047.

[36] HJ 484—2009. Water quality-determination of cyanide-volumetric and spectrophotometry method [S]. (in Chinese)

[37] Q/DYHG 001—2018. Sodium cyanate [S]. (in Chinese)

[38] GB/T 6730.8—2016. Iron ores-determination of iron(II) content−Potassium dichromate titrimetric method [S]. (in Chinese)

[39] YU Hai-yan, PAN Xiao-lin, DONG Kai-wei, WU Yan. Effect of P addition on mineral transition of CaO−Al_2O_3−SiO_2 system during high-temperature sintering [J]. Transactions of Nonferrous Metals Society of China, 2019, 29: 650−656.

[40] DEAN J A. Lange's chemistry handbook [M]. 13th ed. Beijing: Science Press, 1991. (in Chinese)

[41] MILLER A. CRC handbook of chemistry and physics [M]. 78th ed. Radiation Physics and Chemistry, 1998, 53.

[42] VÄHÄ-SAVO N, DEMARTINI N, ENGBLOM M, BRINK A, HUPA M. The fate of char nitrogen in black liquor combustion — Cyanate formation and decomposition [J]. Industrial and Engineering Chemistry Research, 2015, 54: 2831−2842.

[43] NISHIOKA H, NISHIKAWA M, KATAGI M, TSUCHIHASHI H., MURAOKAB O. Mechanistic studies on the decomposition of sodium cyanide in aqueous solution and in the solid state [J]. Forensic Science International, 2005, 153: 125−131.

[44] KIM Jong-Wan, LEE Hae-Geon. Thermal and carbothermic decomposition of Na_2CO_3 and Li_2CO_3 [J]. Metallurgical and Materials Transactions B−Process Metallurgy and Materials Processing Science, 2001, 32: 17−24.

[45] PATNAIK P. Handbook of inorganic chemicals [M]. The McGraw-Hill Companies, Inc., 2002.

[46] GADZHIEV O B, IGNATOV S K, GANGOPADHYAY S, MASUNOV A E, PETROV A I. Mechanism of nitric oxide oxidation reaction ($2NO+O_2\rightarrow 2NO_2$) revisited [J]. Journal of Chemical Theory and Computation, 2011, 7: 2021−2024.

[47] GROSU Y, FAIK A, ORTEGA-FERNÁNDEZ I, D'AGUANNO B. Natural Magnetite for thermal energy storage: Excellent thermophysical properties, reversible latent heat transition and controlled thermal conductivity [J]. Solar Energy Materials and Solar Cells, 2017, 161: 170−176.

[48] WEI Yun-mei, WANG Fei, LIU Xin, FU Peng-rui, LI Yun-yi. Thermal remediation of cyanide-contaminated soils: Process optimization and mechanistic study [J]. Chemosphere, 2020, 239: 124707.

添加氧化铁高效热解脱除氰化钠

董凯伟[1]，谢 锋[1]，王 伟[1]，畅永锋[1]，陈春林[2]，顾晓薇[3,4]

1. 东北大学 冶金学院，沈阳 110819；
2. CSIRO Minerals Resources, Clayton, Victoria 3168, Australia;
3. 东北大学 资源与土木工程学院，沈阳 110819；
4. 东北大学 智慧水利与资源环境科技创新中心，沈阳 110819

摘 要：提出采用氧化铁催化热解高效除氰。采用 XRD、DSC−TG、化学分析等手段对不同条件下添加和无添加氧化铁高效脱除氰化钠的机理进行研究。未添加氧化铁时，空气条件下，氰化钠在 587.4 °C 开始发生分解；氩气条件下，氰化钠在 879.2 °C 开始发生分解。添加氧化铁时，氩气条件下，大约 60%的氰化钠在 350 °C 热解 30 min 时发生分解；在空气或氧气条件下，当氧化铁与氰化钠质量比为 1:1 时，几乎所有的氰化钠在 350 °C 热解 30 min 内完成脱除。研究表明，催化剂 Fe_2O_3 添加量的增加、除氰温度的升高及除氰时间的延长均有助于氰化钠的脱除。随着氧化铁的添加，氩气条件下，NaCN 与 Fe_2O_3 反应生成 $Na_4Fe(CN)_6$、Na_2CO_3、$NaNO_2$ 和 Fe_3O_4；空气或氧气条件下，NaCN 分解生成 NaCNO、$Na_4Fe(CN)_6$ 和微量的 $NaNO_2$，且形成的 NaCNO 和 $Na_4Fe(CN)_6$ 随后发生分解，生成 Na_2CO_3、CO_2、N_2、FeO_x 和微量的 NO_x。

关键词：氰化物脱除；热分解；氧化铁；催化氧化；氰化钠

(Edited by Bing YANG)